RSC Advances

PAPER

View Article Online
View Journal | View Issue

Cite this: *RSC Adv.*, 2017, **7**, 24353

Controllable synthesis of Ni–Co–Mn multi-component metal oxides with various morphologies for high-performance flexible supercapacitors†

Pingge He, Qun Huang, Boyun Huang and Tengfei Chen*

Ni–Co–Mn multi-component metal oxides with various morphologies for high-performance supercapacitor electrodes were controllably synthesized on carbon cloth through a facile hydrothermal method followed by a subsequent annealing process. The crystalline structure, morphology and electrochemical property of the metal oxides can be manipulated by simply adjusting the Ni/Co/Mn ratio in the solution. The metal oxide prepared in the solution containing a Ni/Co/Mn ratio of 1/1/2 presents a structure consisting of nanosheets and nanoneedles, and exhibits the highest specific capacitance of 1434.2 F g^{-1} at a current density of 2 mA cm^{-2}, desirable rate capability and excellent cyclic stability with a capacitance retention of 94% over 3000 cycles. To demonstrate practical application, flexible asymmetric supercapacitors based on such metal oxides were prepared and show high capacitance, low internal resistance, excellent cyclic stability and outstanding flexibility, indicating great potential as high-performance energy storage devices.

Received 13th March 2017
Accepted 22nd April 2017

DOI: 10.1039/c7ra03018e

rsc.li/rsc-advances

1. Introduction

With the extreme increase in the energy demand and wide application of electric vehicles, renewable and green energy have elicited great attention[1] but how to effectively utilize and store energy for practical applications still remains challenging.[2] Supercapacitors, with fast power delivery, high rate capability and stable cycle life, show great promise as next-generation energy storage systems, complementing and even replacing batteries in many areas.[3] Great efforts have been made to develop novel electrode materials, which play an essential role in the electrochemical performance of supercapacitors.[4,5] Particularly, transition metal oxides such as NiO,[6,7] Co_2O_3 [8,9] and MnO_2 [10,11] are considered as promising candidates as electrodes for supercapacitors because of their widely available resources, high theoretical pseudocapacitance and low toxicity.[5,12] Recently, a novel binary metal oxide $NiCo_2O_4$ has attracted much attention. Compared to traditional single-component metal oxides, such binary metal oxides exhibit better electrochemical activity and higher electronic conductivity, at least two orders of magnitude higher than that of the single component nickel or cobalt oxides.[13–15]

It is well known that the metal component in oxides greatly affects the performance of final products.[16] For $NiCo_2O_4$, it could be simply regarded as one of the cobalt atoms in Co_2O_3 substituted by a nickel atom.[13] Nickel in oxides enhances electrochemical activity, leading to highly pseudocapacitive behaviour,[17] while cobalt can effectively improve the conductivity of oxides, resulting in stable electrochemical performance.[18] The synergistic effect between Ni and Co significantly contributes to the outstanding performance of supercapacitors based on $NiCo_2O_4$ electrodes.[19–21] The successful achievement of such high-performance electrodes with a homogeneous binary metal oxide in a unitary structure is attributed to the similar atom size between two metal elements and the compatibility of crystalline structure.[13] To further improve the comprehensively electrochemical property of supercapacitors in practical applications, multi-component (>2) metal oxides/hydroxides with a unitary structure are expected to be designed and fully exploited as electrode materials. Our previous work has reported a successful achievement of Ni–Co–Mn oxides/hydroxides and demonstrated their great superiority as supercapacitor electrodes over other transitional metal oxides/hydroxides.[22,23] Mn element possesses a similar atom size to that of Ni or Co. More importantly, Mn exhibits various oxidation states (Mn^{2+}, Mn^{3+}, Mn^{4+}) in oxides,[24] leading to high electrochemical activity for supercapacitor applications.[25] However, rarely has it been reported on effects of Mn on the morphology of Ni–Co–Mn oxides and subsequent influences on the electrochemical properties.

State Key Laboratory of Powder Metallurgy, Central South University, Changsha 410083, China. E-mail: tengfei@csu.edu.cn

† Electronic supplementary information (ESI) available. See DOI: 10.1039/c7ra03018e

In this work, we developed a cost-effective and facile hydrothermal strategy to design and fabricate Ni–Co–Mn oxides with various morphologies and structures on carbon cloth (CC) as binder-free electrodes for high-performance supercapacitor applications. The variety of morphology and structure can be realized by adjusting the Ni/Co/Mn molar ratio in the precursor solution. Moreover, relationships between the morphology, electrochemical performance and the Ni/Co/Mn molar ratio have been thoroughly investigated. The results reveal great influences of Mn on both morphology and electrochemical performance of such multi-component metal oxides. Furthermore, for practical applications, supercapacitors are required to operate well under different deformation situations. Herein, a highly flexible asymmetric supercapacitor consisting of Ni–Co–Mn metal oxide (a Ni/Co/Mn molar ratio of 1/1/2) as positive electrode, electrochemically active CC as negative electrode and KOH/PVA as bifunctional electrolyte and separator. The present asymmetric supercapacitors exhibit high capacitance, excellent cyclic stability and high flexibility, showing great promise as next-generation energy storage systems.

2. Experimental

2.1 Synthesis of Ni–Co–Mn multi-component metal oxides on CC as free-standing electrodes

All reagents used in the experiment were of analytical grade and purchased from Aladdin Industrial Co. Bare CC (1 cm × 4 mm in a rectangular shape) was immersed in an ethanol solution for 5 min to improve the hydrophilicity. The Ni–Co–Mn multi-component metal hydroxide precursors were firstly prepared on CC surface through a hydrothermal process. To investigate the effect of Mn on the final metal oxide, solutions containing $Ni(NO_3)_2$, $Co(NO_3)_2$, $Mn(NO_3)_2$ and urea with different Ni/Co/Mn molar ratios were made that the molar ratios of $Ni(NO_3)_2$, $Co(NO_3)_2$, $Mn(NO_3)_2$ and urea in the solution are 1 : 1 : 1 : 3, 1 : 1 : 2 : 4, 1 : 1 : 3 : 5 and 1 : 1 : 5 : 7, respectively. The solution with CC immersed in was then transferred into a 50 mL Teflon-lined stainless steel autoclave. The autoclave was maintained at 140 °C for 5 h in an electric oven and subsequently cooled to room temperature in air. The samples were washed many times and sonicated to remove excessive metal oxides piled on the CC surface. To obtain Ni–Co–Mn oxides, as-grown hydroxide precursors were heated in a quartz tube furnace from room temperature to 300 °C, annealed at 300 °C for 2 h, and cooled to room temperature naturally under steady N_2 flow. For comparison, $NiCo_2O_4$ grown on CC was also prepared under the same condition in a solution containing $Ni(NO_3)_2$, $Co(NO_3)_2$ and urea as a molar ratio of 1 : 2 : 3. The final metal oxides were labelled as $NiCo_2$, NiCoMn, $NiCoMn_2$, $NiCoMn_3$ and $NiCoMn_5$ corresponding to different Mn concentrations in solutions.

2.2 Fabrication of flexible asymmetric supercapacitors

Asymmetric supercapacitors were assembled by using $NiCoMn_2$/CC as a positive electrode and electrochemically active CC (ACC) as a negative electrode. The polymer gel KOH/PVA was used as a bifunctional electrolyte and separator. Firstly, the KOH/PVA gel electrolyte was prepared (the details of electrolyte preparation are provided in ESI†). Then, a piece of $NiCoMn_2$/CC electrode and a piece of ACC electrode were immersed in the hot dilute polymer electrolyte solution. The dilute solution soaked and penetrated the electrodes well and formed a coating layer on the surface of the electrodes. The electrodes with the electrolyte solution coating on were placed in a fume hood at room temperature to evaporate the excess water. After the KOH/PVA became solidified, the two electrodes were tightly pressed together into one integrated unit.

2.3 Material characterization

The surface morphology of electrodes was characterized by field emission scanning electron microscope (FESEM, Nova Nano 230). The structure and chemical composition of the electrodes were investigated characterized by transmission electron microscopy (TEM, Japan FEM-2100F) combined with energy-dispersive X-ray spectroscopy (EDX) mapping, X-ray diffraction (XRD, D/max 2550) and X-ray photoelectron spectroscopy (XPS K-Alpha 1063, UK Thermo Fisher).

2.4 Electrochemical treatments and characterization

The electrochemical performance was evaluated using an electrochemical workstation (CHI660C). Electrochemical measurements were conducted in a three-electrode configuration at room temperature using 2 M KOH as electrolyte. Multi-component metal oxides grown on CC samples served directly as the working electrode. Pt mesh and standard calomel electrode (SCE) were used as the counter electrode and reference electrode, respectively. Electrochemical impedance spectroscopy (EIS) was conducted using a Modulab (Solartron Analytical) with an amplitude of 5 mV in the frequency ranging from 1 MHz to 0.1 Hz. All electrochemical tests were conducted at room temperature.

3. Results and discussion

To investigate the structure of multi-component metal oxides, X-ray diffraction (XRD) was employed to analyse crystalline structures of metal oxides prepared in solutions with different Ni/Co/

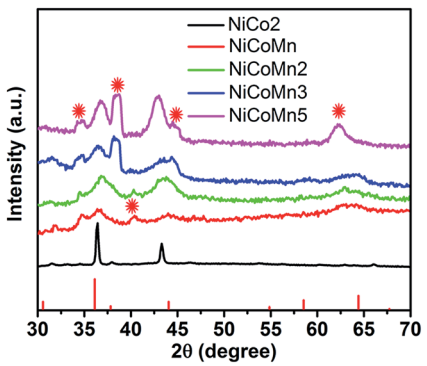

Fig. 1 XRD patterns of multi-component metal oxides prepared in various solutions with different Ni/Co/Mn molar ratios.

Mn ratios. To eliminate CC effects on results, we collected only metal oxide powder for XRD tests. As shown in Fig. 1, for $NiCo_2$ oxide (without Mn), two obvious diffraction peaks are observed at 2θ values of 36.6° and 44.5°, corresponding to (311) and (400) plane reflections of the $NiCo_2O_4$ crystalline structure[26] (with the standard peaks indicated by the red lines in Fig. 1). The sharp diffraction peaks here indicate highly crystal structure of $NiCo_2$ oxide. When Mn was added in the precursor solution (with a Ni/Co/Mn ratio of 1 : 1 : 1), the final metal oxide product presents two more peaks at approx. 35° and 41° in the XRD pattern, and all peaks become much milder compared to that of $NiCo_2$ oxide, indicating the Mn addition alters the crystal structure of final metal oxide products. With increasing concentration of Mn in the solution, the final metal oxide products show a few differences in the peak intensity of XRD patterns. However, when the Ni/Co/Mn ratio reaches 1 : 1 : 3, an obvious peak at approx. 38° and a mild peak at approx. 45° rose in the XRD pattern of $NiCoMn_3$ oxide while the peak at approx. 41° almost disappeared. The XRD pattern of $NiCoMn_5$ oxide is similar to that of $NiCoMn_3$ but the relative intensities of peaks at approx. 41° and 64.6° increase. The significant difference in XRD patterns between these multi-component metal oxides reveals Mn concentration in the precursor solution has an essential effect on the crystalline structure of final metal oxides.[22]

In order to investigate the morphology evolution of multi-component metal oxides with various Ni/Co/Mn molar ratios, SEM images of Ni–Co–Mn oxides are shown in Fig. 2. For comparison, SEM images of $NiCo_2$ oxide on CC are also provided in Fig. 2a and b. Fig. 2a shows a uniform coverage of $NiCo_2$ oxide nanoneedles on CC and such nanoneedles randomly interconnected, forming a network-like structure on carbon fiber surface (see Fig. 2b). With the addition of Mn (a Ni/Co/Mn ratio of 1/1/1), the CC surface shows more dense coverage of NiCoMn oxide nanoneedles (see Fig. 2c) and such NiCoMn oxide nanoneedle arrays with sharp tips are orderly perpendicular to CC surface (see Fig. 2d). However, when the Mn concentration increases (a Ni/Co/Mn ratio of 1/1/2), the final products consist of not only nanoneedles but also nanosheets (see Fig. 2e). From the high-magnification SEM in Fig. 2f, sharp tips of nanoneedles and edges of nanosheets are clearly distinguished. These nanoneedles with sharp tips and nanosheets with sharp edges are expected to facilitate the electrolyte ion transfer to electrode. As the Ni/Co/Mn ratio in precursor solution becomes 1/1/3, all nanoneedles disappear. Instead, final metal oxides present nanosheet structures (see Fig. 2g and h). With a continuous increase of Mn concentration (a Ni/Co/Mn ratio of 1/1/5), the metal oxide nanosheets grow largely and densely on carbon fiber surface (see Fig. 2i and h).

Typical TEM images of NiCoMn, $NiCoMn_2$ and $NiCoMn_3$ oxides are provided in Fig. 3 to achieve a profound understanding of the microstructure. As shown in Fig. 3a, NiCoMn oxide nanoneedles exhibit sharp tips, with a tip diameter of approximately a few nanometers to several tens of nanometers. Fig. 3b clearly displays nanoneedles and nanosheets in $NiCoMn_2$ oxide, consistent with the results from SEM images. However, $NiCoMn_3$ oxides exhibit thin nanosheet structures and the span of individual nanosheet is in a range of several hundred nanometers (see Fig. 2c). The subsequent TEM elemental mapping analysis of typical NiCoMn oxide nanoneedles (see Fig. 3d–h) strongly confirms the homogenous

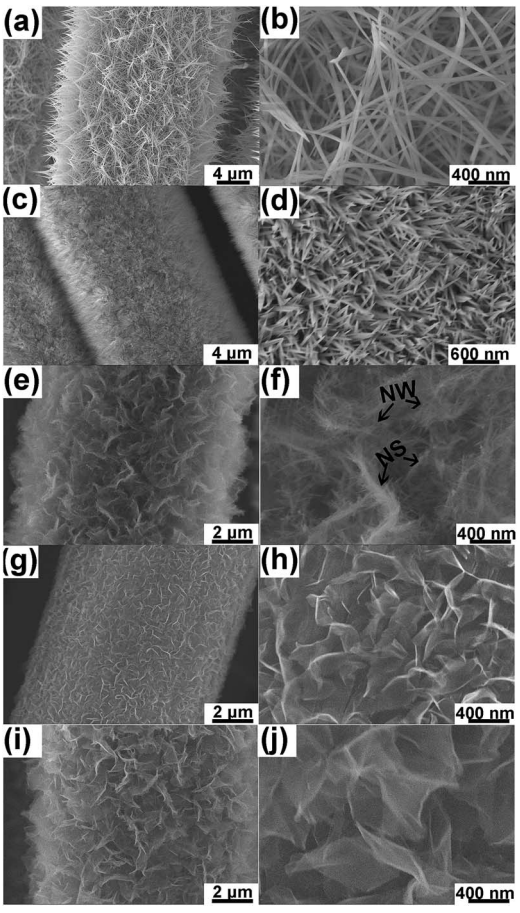

Fig. 2 The SEM images of multi-component metal oxides prepared in various solutions of different Ni/Co/Mn molar ratios. (a and b) $NiCo_2$. (c and d) NiCoMn. (e and f) $NiCoMn_2$. (g and h) $NiCoMn_3$. (i and j) $NiCoMn_5$.

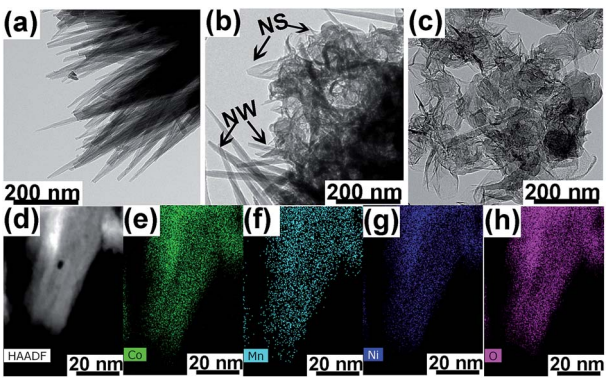

Fig. 3 Typical TEM images of (a) NiCoMn, (b) $NiCoMn_2$ and (c) $NiCoMn_3$ oxides. (d) High-angle annular dark field (HAADF) scanning TEM image of NiCoMn nanoneedles and elemental mapping showing the uniform spatial distribution of mapped elements in the nanoneedles: (e)–(h) Co, Mn, Ni and O maps, respectively.

distribution of Ni, Co, Mn and O elements in the unitary nanoneedle structure. The surface chemical composition of typical $NiCoMn_2$ oxide sample was investigated by XPS and the results are shown in ESI, Fig. S1,† indicating that $NiCoMn_2$ oxide possesses a diverse composition of Ni^{2+}, Ni^{3+}, Co^{2+}, Co^{3+}, Mn^{2+} and Mn^{3+} on the surface, providing more electroactive sites than single- or double-component metal oxides.

The electrochemical performance of multi-component metal oxides with different morphologies was systematically characterized and the related results are provided in Fig. 4. Fig. 4a shows the cyclic voltammetry (CV) curves of bare CC and metal oxide-based electrodes at a fixed scan rate of 20 mV s^{-1} with a voltage window from −0.2 to 0.5 V *vs.* SCE (CV curves of $NiCo_2$, NiCoMn, $NiCoMn_2$, $NiCoMn_3$ and $NiCoMn_5$ oxides at different scan rates are provided in ESI, Fig. S2†). The negligible CV loop area of bare CC indicates the effect of CC substrate on the electrochemical performance of electrodes is ignorable. Two mild redox peaks are observed in the CV curve of $NiCo_2$ oxide, while redox peaks become more obvious after the addition of Mn element. Moreover, the redox peak location of metal oxides varies with different Mn concentrations. The redox peaks in CV curves are mainly associated with the faradaic redox reactions related to M–O/M–O–OH, where M refers to Ni, Co or Mn.[27,28] It is noteworthy that the area of CV loops firstly increases as the Ni/Co/Mn ratio varies from 1/1/0 to 1/1/2 and then decreases with further increasing Mn concentration in the precursor solution. Among these metal oxides, $NiCoMn_2$ oxide exhibits a CV curve with the largest area, revealing the highest capacitance of $NiCoMn_2$ oxide.

Fig. 4b displays the galvanostatic charge/discharge profiles of bare CC and metal oxide-based electrodes at a current density of 2 mA cm^{-2} (charge/discharge profiles of $NiCo_2$, NiCoMn, $NiCoMn_2$, $NiCoMn_3$ and $NiCoMn_5$ oxides at different current densities are provided in ESI, Fig. S3†). The short charge/discharge time for bare CC further confirms the negligible influence of CC substrate on the electrochemical properties of electrodes. The metal oxides with Mn element shows more distinct voltage plateaus compared to $NiCo_2$ oxide and these plateaus match well with the redox peaks observed in the CV curves. Furthermore, the discharge time corresponding to the capacitances of these metal oxides produces the following order: $NiCoMn_2$ > NiCoMn > $NiCoMn_3$ > $NiCoMn_5$ ≈ NiCo. The capacitance calculated from charge/discharge curves (calculation details are provided in ESI†) is plotted as a function of current density in Fig. 4c. At a current density of 2 mA cm^{-2}, the capacitance of $NiCo_2$, NiCoMn, $NiCoMn_2$, $NiCoMn_3$ and $NiCoMn_5$ oxide is 640.6, 1160.8, 1434.2, 914.7, 645.8 F g^{-1}, respectively. The capacitance of metal oxides firstly rises as the Mn concentration increases while decreases with continuously increasing Mn concentration. $NiCoMn_2$ oxide exhibits the highest capacitance among these metal oxides, consistent with the results from CV and charge/discharge curves. As the current density increases from 2 to 15 mA cm^{-2}, all capacitances of metal oxides undergo a continuous attenuation with a capacitance retention of $NiCo_2$, NiCoMn, $NiCoMn_2$, $NiCoMn_3$ and $NiCoMn_5$ oxide to be 87.4%, 85%, 90%, 82.1%, 74%, respectively, at a current density of 15 mA cm^{-2}.

Nyquist plots of these metal oxides recorded from 0.1 Hz to 1 MHz are provided in ESI, Fig. S4.† Long-term cycle lifetime is one of the most critical issues concerning metal oxide-based supercapacitor electrodes. Fig. 4d shows the specific capacitance retention of metal oxides as a function of cycle number during galvanostatic charge/discharge test over 3000 cycles at a current density of 20 mA cm^{-2}. $NiCoMn_2$ oxide sample shows best cyclic stability with 94.3% capacitance retention over 3000 cycles, while the decrease of the specific capacitance for the $NiCoMn_5$ oxide sample during the cyclic test is relatively remarkable. Meanwhile, $NiCo_2$, NiCoMn and $NiCoMn_3$ oxide

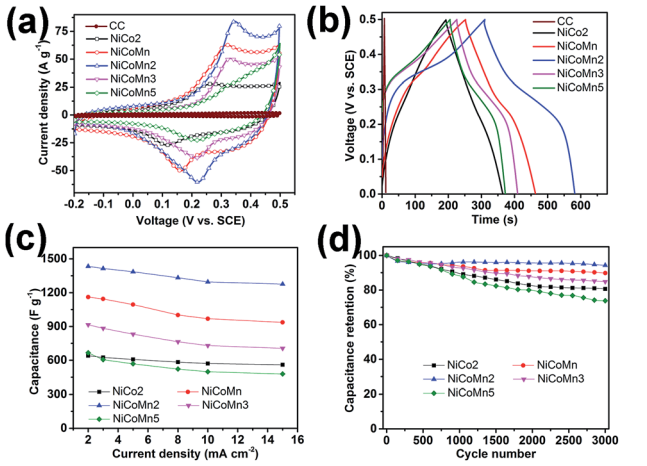

Fig. 4 Electrochemical properties of multi-component metal oxides prepared in various solutions with different Ni/Co/Mn molar ratios. (a) CV curves at a scan rate of 20 mV s^{-1}. (b) Galvanostatic charge/discharge profiles at a current density of 2 mA cm^{-2}. (c) Specific capacitance as a function of current density. (d) Charge/discharge cycling stability test at a current density of 20 mA cm^{-2}.

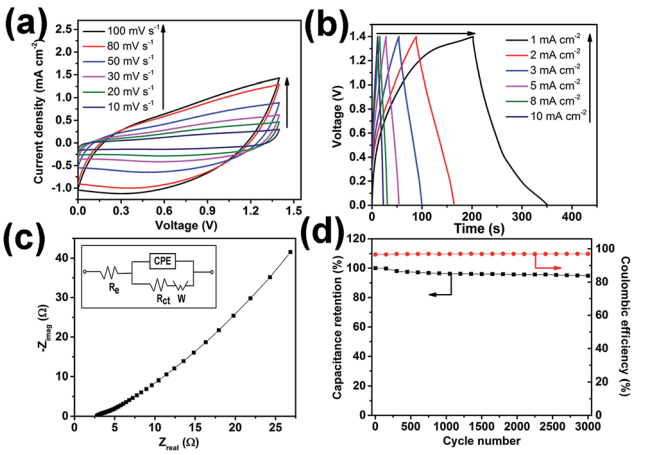

Fig. 5 Electrochemical performance of the asymmetric supercapacitor. (a) CV curves at scan rates from 10 to 100 mV s^{-1} in a voltage window ranging from 0 to 1.4 V. (b) Galvanostatic charge/discharge profiles at current densities from 1 to 10 mA cm^{-2}. (c) Nyquist plot recorded from 0.1 Hz to 1 MHz. (d) Charge/discharge cycling stability test at a current density of 20 mA cm^{-2} and corresponding coulombic efficiencies during the test.

samples show capacitance retentions of 81.6%, 90.3% and 86.4% respectively over 3000 cycles.

The huge differences in electrochemical performance could be attributed to various morphologies of Ni–Co–Mn oxides with different Mn contents. $NiCoMn_2$ oxide exhibits high specific capacitance, good rate capability and excellent cyclic stability, showing great superiority compared to state-of-the-art metal oxide-based materials.[29–31] The outstanding electrochemical performance of $NiCoMn_2$ oxide should be associated with the synergistic effect between Ni, Co and Mn elements, as well as the advantageous structure and the appropriate composition. The appropriate addition of Mn can impel the formation of three-dimensional network structure consisting of nanoneedles and nanosheets, which is particularly beneficial for fast transfer of electrolyte ions to electrode surface, resulting in improved electrochemical performance.

To demonstrate the promise of multi-component metal oxides as supercapacitor electrodes in practical applications, a flexible asymmetric supercapacitor was assembled by utilizing $NiCoMn_2$ oxide on CC as a positive electrode, electrochemically active CC as a negative electrode (details of the electrochemical activation process are provided in ESI, Fig. S5†) and KOH/PAV as a bifunctional electrolyte and separator. The comprehensively electrochemical performance of the device is shown in Fig. 5. CV curves of the asymmetric supercapacitor device at scan rates from 10 to 100 mV s^{-1} shown in Fig. 5a display nearly rectangular shapes, indicating a fast ion diffusion rate and a low internal resistance of the device. The galvanostatic charge/discharge profiles of the asymmetric device at different current densities ranging from 1 to 10 mA cm^{-2} are shown in Fig. 5b. Based on these charge/discharge curves, the areal capacitance of the device is approx. 150 mF cm^{-2} at a current density of 1 mA cm^{-2} (calculated from the equation described in ESI†).

Fig. 5c shows the Nyquist plot for the asymmetric supercapacitor recorded from 0.1 Hz to 1 MHz. The measured impedance spectrum can be fitted by an equivalent circuit[32] consisting of a bulk electrolyte resistance R_e, a charge transfer resistance R_{ct}, a pseudocapacitive element C_p, and a constant phase element (CPE) to represent the double-layer capacitance (see Fig. 5c inset). R_e can be obtained by calculating the real-axis intercept of the impedance spectrum at high frequencies.[33] The R_e value calculated from Fig. 5c for the asymmetric device is approx. 2.8 Ω, indicating low internal resistance. Charge transfer resistance R_{ct}, known as faradaic resistance, is a limiting factor for the specific power and rate capability of supercapacitors.[34] The negligible semicircle in the high frequency region indicates low charge transfer resistance of the device.

As shown in Fig. 5d, the as-prepared device was tested under 3000 galvanostatic charge/discharge cycles at a current density of 20 mA cm^{-2} to demonstrate its cyclic stability. The capacitance of the asymmetric device undergoes a gradual decrease during 3000 cycles with a capacitance retention of 93% at 3 000th cycle. Moreover, the asymmetric supercapacitor exhibits high coulombic efficiencies (>98%) over the 3000 cycles, indicating high charge transfer efficiencies over long term cycling.

For practical application demonstrations, leakage current and self-discharge characteristics of the asymmetric supercapacitors are shown in Fig. 6a and b. The leakage current was measured by keeping the supercapacitor at a constant voltage of 1.4 V for 24 h. The obtained data in Fig. 6a indicates that the leakage current drops rapidly firstly and gradually stabilizes, reaching 0.018 mA after maintaining a constant voltage for 24 h. Such a low leakage current indicates good capacitor performance,[35] which could be attributed to few shuttle reactions caused by the impurities in electrode materials.[36,37]

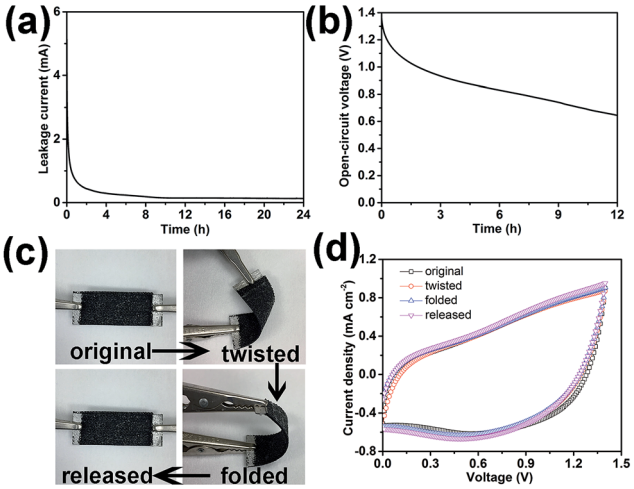

Fig. 6 (a) Leakage current of the asymmetric wire supercapacitor charged to a potential of 1.4 V and kept at the voltage for 24 h. (b) Self-discharge curve of the asymmetric wire supercapacitor under an open-circuit condition for 12 h after being charged at 1.4 V. (c) The photography of the device under different bending states. (d) CV curves measured at a scan rate of 50 mV s^{-1} under the corresponding bending state in (c).

Self-discharge of a supercapacitor refers to the gradual decrease in the voltage across the capacitor that occurs when the capacitor is left unconnected to either a charging circuit or an electrical load, reflecting a loss of efficiency for the capacitor as an energy storage device.[38] The self-discharge profile of the device under an open-circuit voltage condition is shown in Fig. 6b. The asymmetric devices maintain approx. 53.8% of the initial charge potential after 12 h of self-discharge. These leakage current and self-discharge characteristics of the asymmetric supercapacitor confirm that the devices are promising as future energy storage systems.

The flexibility is a significant property for a supercapacitor in practical applications. The high flexibility of as-prepared asymmetric supercapacitor has been demonstrated in Fig. 6c and d. The CV curves of the device under different bending states (see Fig. 6c) have been plotted in Fig. 6d. As obvious, CV curves show few changes under different bending states, even under seriously twisted and folded states, indicating the high flexibility of the as-prepared asymmetric supercapacitor.

4. Conclusions

In conclusion, multi-component metal oxides with various morphologies and compositions were successfully grown on CC

substrates through a facile, cost-effective technique and their electrochemical performance as supercapacitor electrodes was systematically investigated. The results reveal that the microstructure, morphology and electrochemical properties of Ni–Co–Mn oxides can be controlled by adjusting the Ni/Co/Mn molar ratio in precursor solutions. With a Ni/Co/Mn molar ratio of 1/1/2, the final metal oxide consisting of nanosheets and nanoneedles exhibits excellent electrochemical performance with high specific capacitance of 1434.2 F g^{-1}, favourable rate capability and outstanding cyclic stability. The superior performance is attributed to the synergistic effect between Ni, Co and Mn elements, as well as the advantageous structure and the appropriate composition. Furthermore, flexible asymmetric supercapacitors based on such multi-component metal oxides were prepared and exhibited high capacitance, low internal resistance, desirable cyclic stability and outstanding flexibility, showing great promise as next-generation smart energy storage systems.

Acknowledgements

The authors gratefully acknowledge support from the National Natural Science Foundation of China, (PI: Dr Boyun Huang, Grant: No. 51021063) and National High-tech Research & Development Program of China (863 Program) No. 2012AA03A207.

Notes and references

1 J. A. Turner, *Science*, 1999, **285**, 687–689.
2 L. L. Zhang and X. Zhao, *Chem. Soc. Rev.*, 2009, **38**, 2520–2531.
3 J. R. Miller and P. Simon, *Science Magazine*, 2008, **321**, 651–652.
4 P. Simon and Y. Gogotsi, *Nat. Mater.*, 2008, **7**, 845–854.
5 G. Wang, L. Zhang and J. Zhang, *Chem. Soc. Rev.*, 2012, **41**, 797–828.
6 J. W. Lee, T. Ahn, J. H. Kim, J. M. Ko and J.-D. Kim, *Electrochim. Acta*, 2011, **56**, 4849–4857.
7 D. U. Lee, J. Fu, M. G. Park, H. Liu, A. Ghorbani Kashkooli and Z. Chen, *Nano Lett.*, 2016, **16**, 1794–1802.
8 S. K. Meher and G. R. Rao, *J. Phys. Chem. C*, 2011, **115**, 15646–15654.
9 J. Wang, W. Dou, X. Zhang, W. Han, X. Mu, Y. Zhang, X. Zhao, Y. Chen, Z. Yang and Q. Su, *Electrochim. Acta*, 2017, **224**, 260–268.
10 Z. Fan, J. Yan, T. Wei, L. Zhi, G. Ning, T. Li and F. Wei, *Adv. Funct. Mater.*, 2011, **21**, 2366–2375.
11 I. Ryu, H. Yoon, S. J. Ahn and S. Yim, *RSC Adv.*, 2016, **6**, 102814–102820.
12 A. S. Aricò, P. Bruce, B. Scrosati, J.-M. Tarascon and W. Van Schalkwijk, *Nat. Mater.*, 2005, **4**, 366–377.
13 Z. Wu, Y. Zhu and X. Ji, *J. Mater. Chem. A*, 2014, **2**, 14759–14772.
14 Y. Zhang, L. Li, H. Su, W. Huang and X. Dong, *J. Mater. Chem. A*, 2015, **3**, 43–59.
15 F. Yang, J. Yao, F. Liu, H. He, M. Zhou, P. Xiao and Y. Zhang, *J. Mater. Chem. A*, 2013, **1**, 594–601.
16 Y.-M. Wang, X. Zhang, C.-Y. Guo, Y.-Q. Zhao, C.-L. Xu and H.-L. Li, *J. Mater. Chem. A*, 2013, **1**, 13290–13300.
17 S.-I. Kim, J.-S. Lee, H.-J. Ahn, H.-K. Song and J.-H. Jang, *ACS Appl. Mater. Interfaces*, 2013, **5**, 1596–1603.
18 C. Yuan, L. Yang, L. Hou, L. Shen, X. Zhang and X. W. D. Lou, *Energy Environ. Sci.*, 2012, **5**, 7883–7887.
19 R. Wang and X. Yan, *Sci. Rep.*, 2014, **4**, 3712.
20 L. Yu, G. Zhang, C. Yuan and X. W. D. Lou, *Chem. Commun.*, 2013, **49**, 137–139.
21 G. Zhang and X. W. D. Lou, *Adv. Mater.*, 2013, **25**, 976–979.
22 G. Xiong, P. He, L. Liu, T. Chen and T. S. Fisher, *Frontiers in Energy Research*, 2015, **3**, 39.
23 G. Xiong, P. He, L. Liu, T. Chen and T. S. Fisher, *J. Mater. Chem. A*, 2015, **3**, 22940–22948.
24 C.-C. Hu and T.-W. Tsou, *Electrochem. Commun.*, 2002, **4**, 105–109.
25 W. Wei, X. Cui, W. Chen and D. G. Ivey, *Chem. Soc. Rev.*, 2011, **40**, 1697–1721.
26 C. Yuan, J. Li, L. Hou, X. Zhang, L. Shen and X. W. D. Lou, *Adv. Funct. Mater.*, 2012, **22**, 4592–4597.
27 F. Zhang, C. Yuan, X. Lu, L. Zhang, Q. Che and X. Zhang, *J. Power Sources*, 2012, **203**, 250–256.
28 J. Yan, Z. Fan, T. Wei, W. Qian, M. Zhang and F. Wei, *Carbon*, 2010, **48**, 3825–3833.
29 C. Wang, Y. Xi, C. Hu, S. Dai, M. Wang, L. Cheng, W. Xu, G. Wang and W. Li, *RSC Adv.*, 2015, **5**, 107098–107104.
30 N. Padmanathan and S. Selladurai, *RSC Adv.*, 2014, **4**, 8341–8349.
31 J. Gomez and E. E. Kalu, *J. Power Sources*, 2013, **230**, 218–224.
32 B. Conway, *Electrochemical supercapacitors: scientific fundamentals and technological applications*, Springer Science & Business Media, New York, 1999.
33 J. Gamby, P. Taberna, P. Simon, J. Fauvarque and M. Chesneau, *J. Power Sources*, 2001, **101**, 109–116.
34 W. Zhu, Z. Lu, G. Zhang, X. Lei, Z. Chang, J. Liu and X. Sun, *J. Mater. Chem. A*, 2013, **1**, 8327–8331.
35 A. Fuertes, G. Lota, T. Centeno and E. Frackowiak, *Electrochim. Acta*, 2005, **50**, 2799–2805.
36 G. Xiong, C. Meng, R. G. Reifenberger, P. P. Irazoqui and T. S. Fisher, *Adv. Energy Mater.*, 2014, **4**, 1300515–1300524.
37 H. Wada, K. Yoshikawa, S. Nohara, N. Furukawa, H. Inoue, N. Sugoh, H. Iwasaki and C. Iwakura, *J. Power Sources*, 2006, **159**, 1464–1467.
38 B. W. Ricketts and C. Ton-That, *J. Power Sources*, 2000, **89**, 64–69.

